

Manganese and iron-doped yttrium borate as an excellent multifunctional inorganic material

Pankaj Gupta^{1,*†}, Mohit Sahni^{2,*†}

¹ Department of Chemistry and Biochemistry, SBSR, Sharda University, Uttar Pradesh 201310, India

² Department of Physics, SBSR, Sharda University, Uttar Pradesh 201310, India

* **Corresponding author:** Pankaj Gupta, pankaj.chemistry2019@gmail.com; Mohit Sahni, mohit.sahni@sharda.ac.in

† Both the authors have equal contribution.

ARTICLE INFO

Received: 24 September 2023

Accepted: 26 October 2023

Available online: 12 December 2023

doi: 10.59400/mtr.v1i1.377

Copyright © 2023 Author(s).

Materials Technology Reports is published by Academic Publishing Pte. Ltd. This article is licensed under the Creative Commons Attribution 4.0 International License (CC BY 4.0).
<https://creativecommons.org/licenses/by/4.0/>

ABSTRACT: Manganese and iron-doped π -YBO₃ have been synthesized using a modified epoxide-mediated gel method. The PXRD pattern evaluated the formation of the desired phase and the structural changes. EDS spectra determined the elemental analysis of undoped and doped samples. Raman spectra observed the stretching and bending modes of B-O bonds. The direct band gaps for doped samples were 1.47 and 2.07 eV, respectively, lower than the band gap value of 5.81 eV for π -YBO₃. The green and blue indigo emission bands were observed in the photoluminescence spectra. Doped samples showed good magnetic properties as they are antiferromagnetic and ferromagnetic at low temperature (T = 5 K) M-H plot and SQUID measurement. An indigenously built Sawyer-Tower circuit is used to measure ferroelectric hysteresis. Photodegradation studies of RhB were conducted under UV-visible irradiation.

KEYWORDS: borate; sol-gel; magnetic; photocatalytic; ferroelectric; phosphor

1. Introduction

Transition metal borates have recently attained enormous attention due to their significant properties and potential applications^[1-3]. Transition metal borates can be classified into metal orthoborates and metal oxyborates. The metal-rich oxyborates, containing six coordinated metal ion of mixed valence and trigonal planar BO₃³⁻ unit, adopts two warwickite and pinakiolite type structure^[4], and the metal: borate ratio of warwickite is 2:1. In contrast, pinakiolite type has a ratio of 3:1. The mixture of divalent and trivalent metal ions, the composition M₂^{II}M^{III}OBO₃ and M₂^{II}M^{III}O₂BO₃, where metals are iron, cobalt and manganese, can cause the formation of homometallic oxyborates and mixed valence in solid state. The known homometallic oxyborates are manganese oxyborates (Mn₂OBO₃ and Mn₂^{II}Mn^{III}O₂BO₃), iron oxyborates (Fe₂OBO₃ and Fe₂^{II}Fe^{III}O₂BO₃) and cobalt oxyborates (Co₂OBO₃ and Co₂^{II}Co^{III}O₂BO₃) which adopt warwickite and pinakiolite structure^[4-7].

The name warwickite is applied to an unusual family of orthorhombic minerals having space group *Pnma* and ideal composition (M₂O₃BO₃ (M = Mn²⁺, Fe³⁺, Mg²⁺, Ti⁴⁺, and Al³⁺)), warwickite structure was first investigated by Takeuchi et al. in 1950 having composition (Mg,Fe)_{1.5}Ti_{0.5}OBO₃^[4]. Mg₂InBO₅ belongs to the category of M₃BO₅, having a ludwigite structure with a space group of *Pbam*. The M₃BO₅ (where M can be divalent ions such as Mg²⁺, Fe²⁺, Co²⁺, Ni²⁺ and Zn²⁺ or tri- and tetravalent ions as Al³⁺,

V^{3+} , Cr^{3+} , Mn^{3+} , Fe^{3+} , Ga^{3+} , Mn^{4+} , Sn^{4+} , Ge^{4+} , Zr^{4+} and Ti^{4+}) belongs to oxyborate family having ludwigite type structure has already been studied in the past. These all materials such that the cations (transition metal ions) are distributed over four crystallographic distinct octahedral sites, but in some cases, two different atoms can occupy the complementary sites^[8,9]. Rare earth ortho-borates show excessive polymorphism, where most structures have explicitly been determined. The following is a survey of previous work^[10-13]. Levin et al.^[14] 1961 described the vaterite type- orthoborate π -REBO₃ (RE: Y, Nd, Sm-Lu). The structure of π -REBO₃ was proposed to be hexagonal with a coordination number greater than three. A new phase μ -YBO₃ was proposed, which was isostructural with vaterite form and possibly in a pseudohexagonal phase. Newnham et al.^[15] considered two hexagonal structures of π -YBO₃, one distorted with the space group of $P6_3/mmc$ and the other ordered with a space group of $P6_3/mcm$. In both structures, rare earth ions were coordinated with eight oxygen atoms, forming a distorted cube. Spectroscopic techniques such as IR, NMR and Raman studies of π -ortho-borates confirmed the tetrahedral coordination of boron in the $B_3O_9^-$ ring^[16-20]. The hexagonal space group $P6c2$ at low temperatures was proposed by Bradley et al.^[21], and at high temperatures, it described the $P6_322$ space group. In 1977, the pseudohexagonal model for π -YBO₃ orthoborate was proposed by Morgan et al.^[13], and it favoured the pseudowollastonite-type structure over the vaterite type. In 1997, Chadeyron et al.^[22] restudied the structure of π -YBO₃ using single-crystal diffraction techniques where hexagonal cell, $a = 3.776 \text{ \AA}$ and $c = 8.806 \text{ \AA}$ with space group of $P6_3/m$ was observed. Ren et al.^[23] introduced two other space groups for π - and μ -REBO₃, where π -YBO₃ was identified as a sub cell of a rhombohedral structure. In this way, a fully ordered structure in the rhombohedral space group $R32$ was accomplished. The study results of Cohen-Adad et al.^[24] in 2000 were consistent with all possible hexagonal space groups $P6_3/mmc$, $P6c2$, $P6_3/mcm$ and $P6_3/m$, while the best agreement could be accounted for in $P6c2$. For μ -GdBO₃, hexagonal space group $P6_322$ was assumed. Lin et al.^[12] surveyed the powder data of the $Y_{0.92}Er_{0.02}BO_3$ sample by neutron diffraction, and it was found that a monoclinic structure was observed with space group of $C2/c$ for both low- and high-temperature. In 2008, Hosokawa et al.^[25] presented the space group $P6_3/m$ for orthoborate powder synthesized by gyrothermal reaction, which was previously determined by Chadeyron et al.^[22]. We know that literature has yet to be published on doping transition metals in YBO₃. The use of the sol-gel process is quite beneficial for creating superior materials. The result of the sol-gel method is an improvement in the processing of traditional materials and their properties, as well as the synthesis of new materials. Due to its low-temperature nature, the organic-inorganic hybrids sol-gel technique is beneficial for creating high-performance liquid chromatography. The following benefits of the sol-gel technique are Easy procedure, the creation of highly pure products, the efficiency of synthesis is very high, more thorough surface coverage, the creation of low-cost and high-quality materials, etc.^[26]. In the present study, transition metal doped YBO₃ has been synthesized by epoxide gel route. Following this, photoluminescence, magnetic, ferroelectric, and photocatalytic properties have been studied thoroughly. In the present study, transition metal doped YBO₃ has been synthesized by epoxide gel route. Following this, photoluminescence, magnetic, ferroelectric, and photocatalytic properties have been studied thoroughly.

2. Experimental

2.1. Synthesis

To synthesize π -YBO₃, $YCl_{3.6}H_2O$ (99.9%, Sigma Aldrich), H_3BO_3 (99.9%, BDH) and Propylene Oxide (99%, Alfa Aesar, Massachusetts) as the starting materials, we dissolved 0.3056 g (1 mmol) of $YCl_{3.6}H_2O$ in 5 mL of absolute ethanol and 0.061 g of H_3BO_3 (1 mmol), and constantly stirred the

mixture at room temperature. Then, we added 0.69 mL (10 mmol) of propylene oxide drop by drop while stirring the solution. After a few minutes of ultrasonication, the mixture produced a colourless xerogel. We calcined the samples in a muffle furnace at 900 °C for 4 h, with the heating rate set to 20 °C/min. Finally, we allowed the samples to cool naturally to room temperature by turning off the furnace^[27].

Use 0.0192 g (10 mmol) $\text{MnCl}_{2.4}\text{H}_2\text{O}$ (99%, Alfa Aesar), 0.0410 g (10 mmol) $\text{Fe}(\text{NO}_3)_3 \cdot 9\text{H}_2\text{O}$ (98%, CDH), 0.281 g (0.9 mmol) $\text{YCl}_{3.6}\text{H}_2\text{O}$ and 0.061 g H_3BO_3 with 0.69 mL (10 mmol) of propylene oxide to produce xerogels of composition of $\text{Y}_{0.90}\text{M}_{0.10}\text{BO}_3$ ($\text{M} = \text{Mn}^{2+}$ and Fe^{2+}) following the same procedure described for the synthesis of $\pi\text{-YBO}_3$.

2.2. Characterization

A high-resolution Bruker D-8 Advanced X-ray diffractometer was used to record the powder X-ray diffraction (PXRD) patterns. The obtained PXRD data was subjected to structure refinement via the Le Bail method, which used TOPAS3 software. Renishaw spectrometer was adopted to record the Raman spectra using a microscope system operating with an Nd: YAG laser ($\lambda = 532$ nm). Diffuse reflectance spectra were collected for the samples on a Perkin-Elmer Lambda-35 UV-visible spectrophotometer with an attached integrating sphere, taking BaSO_4 as the reference transformed to absorbance via selecting KM Function to perform this. The conventional excitation and emission spectral measurements of the samples were performed adopting Horiba Jobin Yvon Fluorolog-modular spectrofluorometer at room temperature with a continuing-wave xenon lamp source and Cary Eclipse Fluorescence Spectrophotometer G9800AA. Low-temperature magnetic measurements were recorded using MPMS (Magnetic Properties Measurement System) Excel manufacturing quantum design USA in temperatures ranging between 5 to 320 K under an applied field of ± 1 Tesla. Magnetization measurements were performed using a vibrating sample magnetometer (Magnetic Properties Measurement System excel manufacturing quantum design USA) at 5 K and 300 K under an applied field of ± 7 Tesla. An indigenously built Sawyer-Tower circuit was used to measure the ferroelectric hysteresis, and a lock-in amplifier drove the circuit. Further, a photodegradation study of dye molecules was done in the presence of a catalyst in an immersion type, in-house fabricated reactor under UV-visible radiation adopting a 125 W capacity mercury vapour lamp (Philips, India). A solid sample (50 mg) was added to a 10 μM aqueous solution of RhB (pH ~ 7) dye, formed by adopting double distilled water. Firstly, the suspension was stirred under the dark for almost 20 min to attain equilibrium, then turned on the UV-visible radiation and shined on the suspension. A 5–6 mL quantity of aliquots was withdrawn periodically from the reaction mixture. Then, solutions were centrifuged, and the concentration of the solution was obtained by measuring the absorbance at $\lambda_{\text{max}} = 556$ nm for (Rh-B) using a UV-visible spectrometer (Shimadzu UV-1601).

PXRD patterns of 10% manganese and iron-doped $\pi\text{-YBO}_3$, were compared with those of pure $\pi\text{-YBO}_3$, in **Figure 1**. The xerogel is amorphous, and the calcined product exhibited reflections that matched well with hexagonal $\pi\text{-YBO}_3$, regarding position and intensity profile (JCPDS File No. 83-1205).

The PXRD pattern of this sample was successfully refined using the Le-Bail method in the $P6_3/m$ space group. The resulting lattice parameters were $a = 3.7756$ (15) and $c = 8.8138$ (25) with no uncounted reflections^[15,16,22,25]. The crystallite size (D) was estimated to be 27 nm using Scherrer's formula $D = 0.89 \lambda / \beta \cos\theta$, (where λ is the wavelength of the X-ray, θ is the diffraction angle, and β is half peak width). The

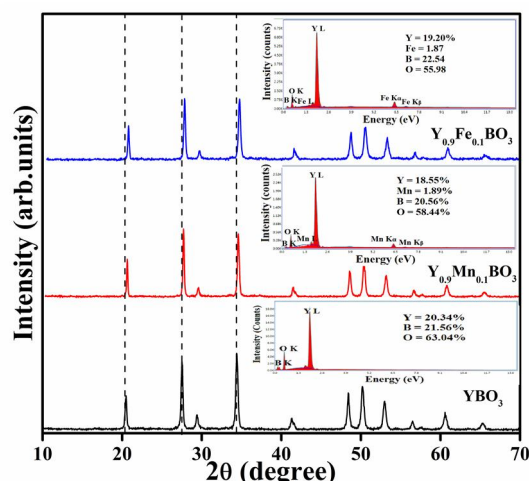


Figure 1. PXRD patterns of product calcination of xerogels from the attempts to make π -YBO₃, manganese and iron doped π -YBO₃, samples. Inset showing the EDS spectra.

doped samples showed peaks only about hexagonal π -YBO₃, with no additional reflections and a systematic shifting of the diffracted peaks toward higher 2θ values was observed. From the Le-Bail refinement of the PXRD pattern, we derived unit cell constants of $a = 3.7701$ (18) and $c = 8.8025$ (11) Å for the manganese-doped sample, $a = 3.7616$ (20) and $c = 8.8011$ (18) Å for the iron-doped sample (**Figure 2**). This suggests the inclusion of smaller-sized manganese (0.83 Å) and iron (0.78 Å) for Y³⁺ in six-fold coordination. The crystallite size of π -YBO₃, increased with the doping of transition metal ions, with crystallite sizes of 36 nm and 38 nm deduced for the manganese and iron-doped samples, respectively. EDS analysis of the π -YBO₃ sample showed that approximately 21%, 22%, and 63% of Y, B, and O were present in the sample, respectively, which was close to the expected ratio of 1:1:3. For the doped samples, 10% manganese and iron were confirmed to be present about the amount of yttrium.

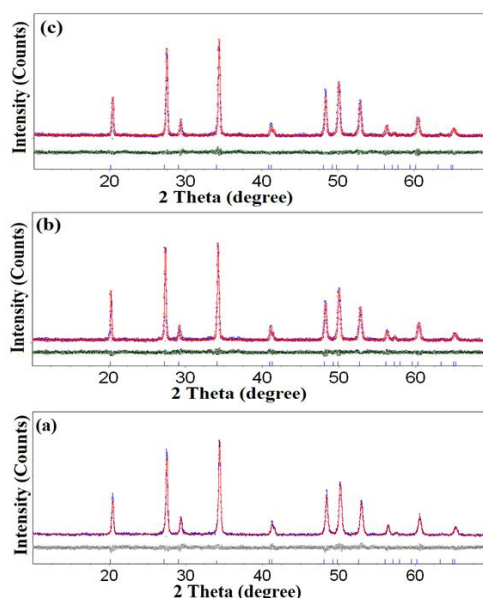


Figure 2. Le-Bail refinement of (a) π -YBO₃, (b) π -Y_{0.90}Mn_{0.10}BO₃ and (c) π -Y_{0.90}Fe_{0.10}BO₃.

Raman spectra of Mn²⁺ and Fe²⁺ doped π -YBO₃ samples have been compared with π -YBO₃, in **Figure 3**. Translations of Y³⁺, B₃O₉ units and vibrational modes of B₃O₉ units within the structure contribute to the bands visible between 180 and 250 cm⁻¹. Moreover, the existence of B₃O₉ rings was

attributed to the bands present at 414 and 513 cm^{-1} . B-O-B bending of the BO_4 units and $\text{B}_3\text{O}_9^{9-}$ borate ring deformation modes were visible at 615 and 839 cm^{-1} . Stretching vibration of tetrahedral BO_4 groups exists as a part of the $\text{B}_3\text{O}_9^{9-}$ ring displayed as a band at 1006 cm^{-1} [27–29]. All the Raman peaks shifted toward lower values for Mn^{2+} and Fe^{2+} doped samples, confirming their incorporation.

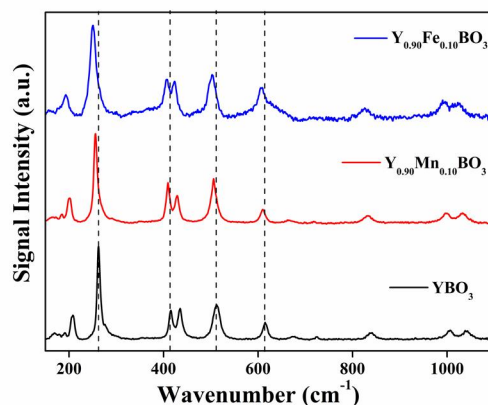


Figure 3. Raman spectra of undoped and doped π - YBO_3 .

UV-visible spectra of Mn^{2+} and Fe^{2+} doped π - YBO_3 are presented in Figure 4. The band centred at 235, 360, 402 and 498 nm for the manganese doped samples corresponded to transitions from ${}^6\text{A}_{1g}(\text{S})$ to ${}^4\text{A}_{1g}(\text{F})$, ${}^4\text{T}_{2g}(\text{D})$, ${}^4\text{E}_g(\text{D})$ and ${}^4\text{T}_{1g}(\text{G})$, respectively[30]. On the other hand, the broad band centred at 534 nm and 885 nm for the iron doped π - YBO_3 corresponded to ${}^5\text{A} \rightarrow {}^5\text{E}$ and ${}^6\text{A}_1 \rightarrow {}^4\text{T}_1$ (${}^4\text{G}$) transitions of iron, respectively[31].

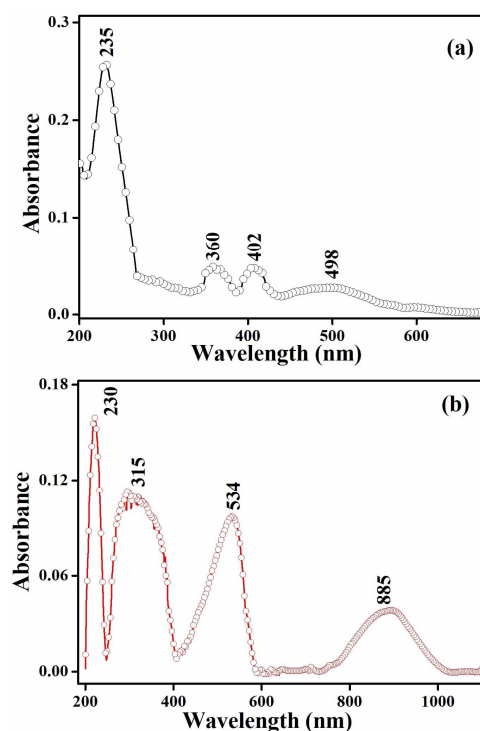


Figure 4. UV-visible spectra for (a) π - $\text{Y}_{0.90}\text{Mn}_{0.10}\text{BO}_3$ and (b) π - $\text{Y}_{0.90}\text{Fe}_{0.10}\text{BO}_3$.

The direct band gaps for Mn^{2+} and Fe^{2+} doped samples, calculated using Tauc plot $((\alpha h\nu)^2$ (eV/cm^2) versus $h\nu$ (eV)), were 1.47 and 2.07 eV, respectively. They were lower than the value of 5.81 eV for

π -YBO₃. Pure π -YBO₃ was off-white, whereas brown and reddish-brown colours were acquired by Mn²⁺ and Fe²⁺ doped samples (Figure 5). PL spectra of Mn²⁺ and Fe²⁺ doped π -YBO₃ have been presented in Figure 6(a). Blue indigo emissions at 412, 438 and 454 nm were observed for the Fe²⁺ doped sample^[32]. The green emission band in the region of 500 nm to 630 nm was assigned to the ⁶A_{1g} (⁶S) → ⁴T_{1g} (⁴G) transition of Mn²⁺ doped π -YBO₃^[33].

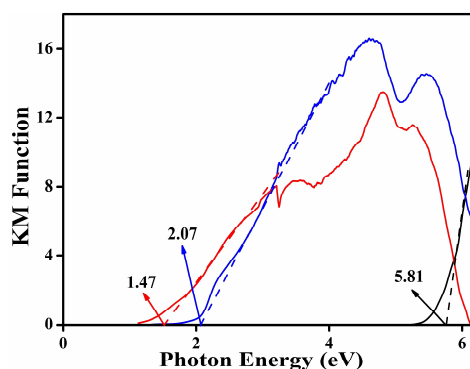


Figure 5. Bandgap estimation for π -YBO₃ (Black), π -Y_{0.90}Mn_{0.10}BO₃ (Red) and π -Y_{0.90}Fe_{0.10}BO₃ (Blue).

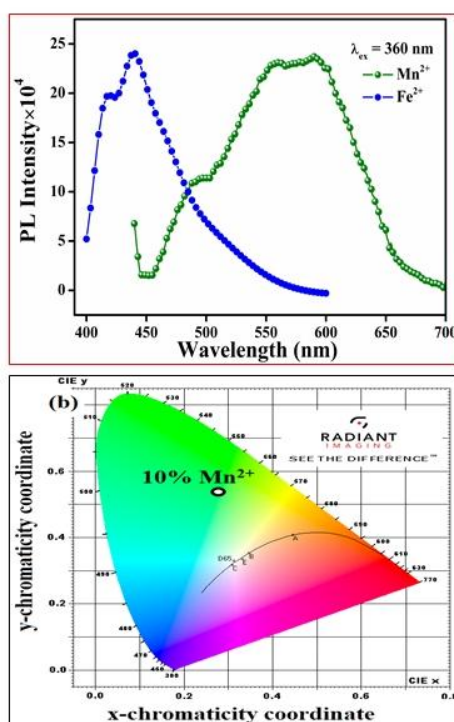


Figure 6. (a) PL spectra of π -Y_{0.90}Mn_{0.10}BO₃ and π -Y_{0.90}Fe_{0.10}BO₃ and (b) CIE coordinate of colour intensity of Mn²⁺ doped π -YBO₃.

The CIE 1931 XY coordinate plot for the Mn²⁺ doped sample as per their emission maxima has been presented in Figure 6(b), which fell in the green region.

3. Magnetic properties

In Figure 7(a), the Magnetic properties of π -Y_{0.90}Mn_{0.10}BO₃ have been investigated at 200 K. The sample exhibited a hysteresis loop with an immense coercivity value ($H \approx 31.5$ K Oe), indicating ferromagnetic solid ordering^[34]. The magnetic susceptibility of the sample was studied in zero field-cooled (ZFC) and field-cooled (FC) conditions. The ZFC measurements revealed antiferromagnetic ordering with a Neel temperature (T_N) of 108 K. Below T_N , the sample showed antiferromagnetic

behaviour, while above T_N , it showed paramagnetic behaviour. On the other hand, FC measurements showed ferromagnetic behaviour below Curie temperature ($T_C \approx 171$ K), indicating the existence of large domains in the same direction. These results provide important insights into the magnetic properties of π - $Y_{0.90}Mn_{0.10}BO_3$ at 200 K.

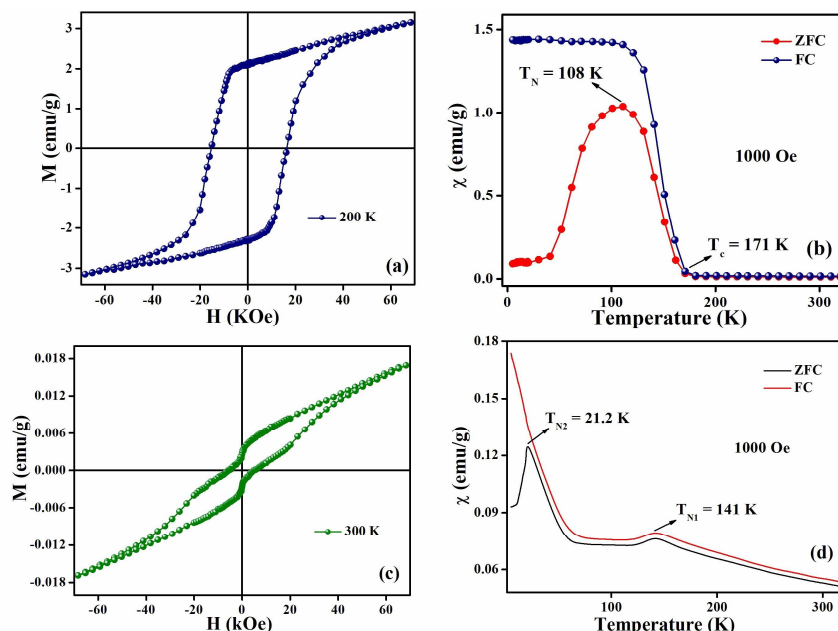


Figure 7. (a) and (c) show the magnetization versus magnetic field for π - $Y_{0.90}Mn_{0.10}BO_3$ and π - $Y_{0.90}Fe_{0.10}BO_3$. (b) and (d) represent the variation of magnetic susceptibility with temperature under zero field and at an applied field of 1000 Oe for π - $Y_{0.90}Mn_{0.10}BO_3$ and π - $Y_{0.90}Fe_{0.10}BO_3$.

The zero field-cooled (ZFC), and field cooled (FC) samples showed significant differences at low temperatures in the curve. This could be due to an inhomogeneous mixture of ferromagnetic and antiferromagnetic ordering in the sample and frustration in the lattice. Similar magnetic behaviour has been reported in the literature^[35,36]. **Figure 7(c)** shows iron-doped samples' magnetization versus magnetic field. A small hysteresis loop suggests the presence of antiferromagnetic ordering in the sample at 300 K^[37]. The magnetic susceptibility of π - $Y_{0.90}Fe_{0.10}BO_3$ under ZFC and FC conditions has been presented in **Figure 7(d)**. For Fe^{2+} doped π - YBO_3 , the magnetic susceptibility was increased with a decrease in temperature from 320 K and exhibited a small cusp at around 141 K, indicating the presence of antiferromagnetic ordering. Below 133 K, magnetic susceptibility was again increased and exhibited a curve around 21.2 K before falling rapidly as the temperature approached 5 K. The cooled (FC) plot showed similar behaviour above 21.2 K temperature. The bifurcation in both ZFC and FC curves above 141 K might be due to the anisotropy in the system, which appeared well above T_N ^[38,39]. The ZFC/FC bifurcation also exhibited local spin or anti/ferromagnetic domain growth clustering. Such bifurcation behaviour was noticed for Fe_3BO_3 in the literature^[40].

The magnetic moment value for the manganese doped sample was plotted with a temperature range of 5 K to 300 K (**Figure 8**). Magnetic moment increased with temperature up to 74 K and showed a decreasing trend. The magnetic moment (μ_{eff}) values were 5.74 BM at 74 K, corresponding to the +2-oxidation state of manganese. This was due to the orientation of domains at low temperatures, which became random at room temperature^[41]. For the iron-doped sample, the magnetic moment increased with temperature. At room temperature, it was found to be 4.81 BM, corresponding to the only value of Fe^{2+} (d^6 configuration, 4 unpaired electrons).

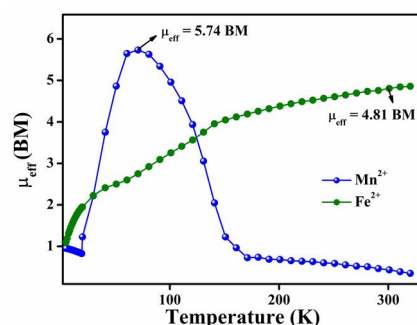


Figure 8. Magnetic moment versus temperature plot for manganese and iron, doped π -YBO₃.

3.1. Ferroelectric properties

The combine P-E loops of Mn²⁺ and Fe²⁺ doped sample at 7 V/cm potential have been shown in **Figure 9**. It was observed that π -YBO₃ doped with Mn²⁺ exhibited ferroelectric polarization, with $P_r \approx 9.52 \times 10^{-2} \mu\text{C}/\text{cm}^2$ as the P-E loop's remnant polarisation value. The iron-doped sample also displayed ferroelectric polarization, with a remnant polarization value of 1.90×10^{-1} at zero electric fields^[37,42].

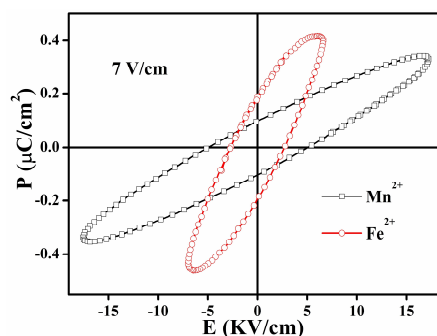


Figure 9. Ferroelectric hysteresis loop (P-E) curve for π -Y_{0.90}Mn_{0.10}BO₃ and π -Y_{0.90}Fe_{0.10}BO₃ at 7 V/cm.

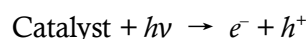
3.2. Photocatalytic properties

The catalytic role of π -Y_{0.90}Mn_{0.10}BO₃ and π -Y_{0.90}Fe_{0.10}BO₃ for the photodegradation of RhB dye solution was studied. Temporal changes in absorbance maxima at $\lambda = 549 \text{ nm}$ (for RhB dye) in the presence of undoped and doped samples after shining with UV-visible radiation have been shown in **Figure 10(a–c)**.

The reduction in intensity of absorbance maxima confirmed their catalytic role in the presence of these samples. Approximately 57%, 93% and 87% of dye was observed to degrade in 90 min of exposure with undoped and doped samples, respectively (**Figure 10(d)**). The concentration of dye was computed using the expression,

$$C = C_0 \exp(-kt)$$

C —concentration of dye at time t , C_0 —concentration at $t = 0 \text{ min}$, k —rate constant and t —time in minutes. Pseudo-first-order rate constants (k) for these experiments employing π -YBO₃, π -Y_{0.90}Mn_{0.10}BO₃ and π -Y_{0.90}Fe_{0.10}BO₃ as catalysts were 9.16×10^{-3} , 3.01×10^{-2} and $2.54 \times 10^{-2} \text{ min}^{-1}$, whereas in the absence of catalyst (photolysis experiments), observed rate constant was found $5.14 \times 10^{-4} \text{ min}^{-1}$ (**Figure 10(e)**). The excitation of electrons from the valance band (VB) to the conduction band (CB) and generation of electron-hole ($e^- - h^+$) pairs is predicted due to the narrow bandgap^[28].



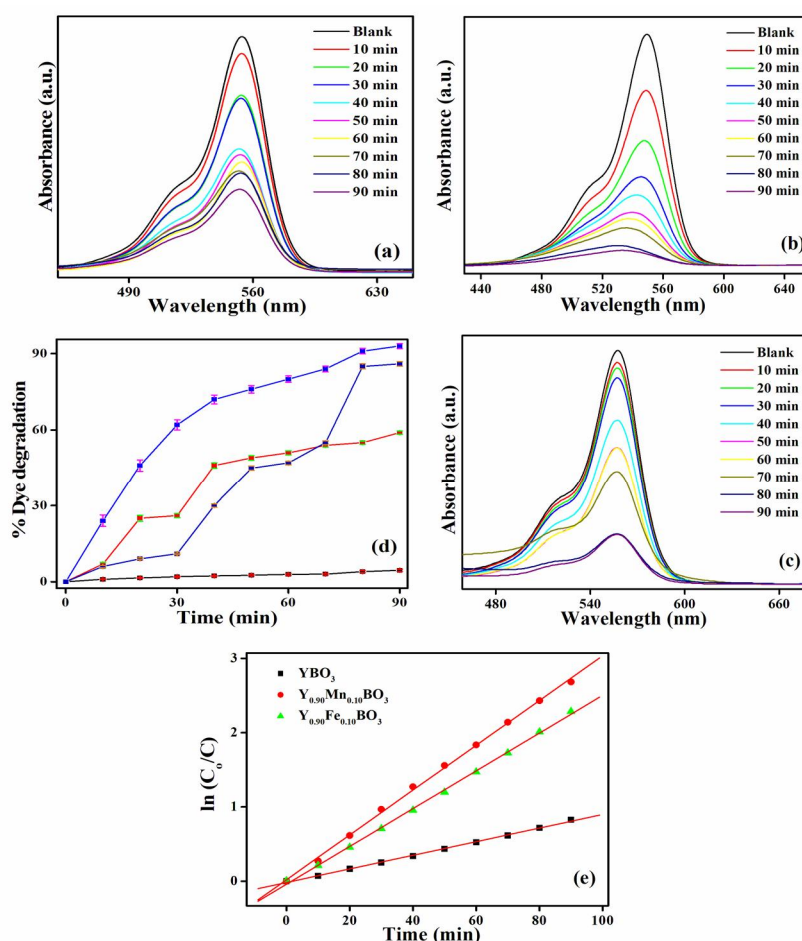
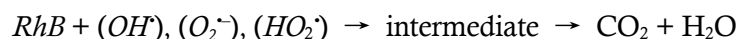


Figure 10. (a–c) Photocatalytic degradation of RhB under UV-visible irradiation, in presence of π -YBO₃, π -Y_{0.90}Mn_{0.10}BO₃ and π -Y_{0.90}Fe_{0.10}BO₃, (d) Dye degradation plot (Black = photolysis, Royal = π -YBO₃, Red = Y_{0.90}Mn_{0.10}BO₃ and Blue = π -Y_{0.90}Fe_{0.10}BO₃) and (e) $\ln(C_0/C)$ plot.

The holes (h^+) generated in the valance band will react with H_2O and hydroxyl anion (OH^-) acting as electron donors to form hydroxide radical (OH^\cdot). In the conduction band, electrons will react with electron acceptor species, i.e., oxygen molecule (O_2) leading to the formation of reactive oxygen anion radical (O_2^\cdot).

Afterwards, reactive hydroperoxyl radical (HO_2^\cdot) will form. At the end, OH^\cdot , O_2^\cdot , HO_2^\cdot radicals will attack the dye molecule, leading to the intermediate with the formation of the final product. Photodegradation of dye through radical mechanism has already been reported in the literature^[28,43].

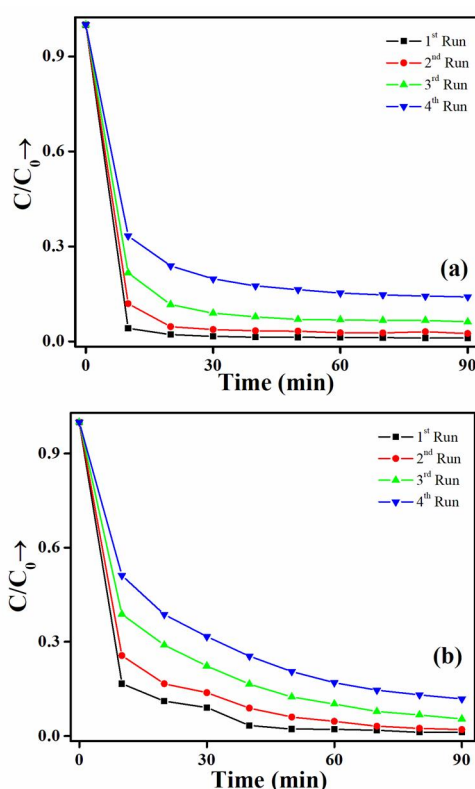


The comparison study of magnetic and photocatalytic properties of our material with other literature is mentioned in the tabular form (Table 1).

To check the stability of our catalyst, we have performed a reusability experiment for the manganese and iron-doped samples (Figure 11). The results show that the catalyst degrades the same amount of dye solution until the 4th run. The high degradation of dye and stability is better performed by the manganese-doped sample over iron.

Table 1. Comparison of performance of manganese and iron doped orthoborate catalyst with the other photocatalyst.

Compound	Dye	Concentration (M)	Rate constant (min^{-1})	Efficiency (%)	Time (min)	Ref.
TiO ₂ (P25)	RhB	2×10^{-5}	5.7×10^{-2}	85	20	[44]
Co _{0.75} Fe _{2.25} O ₄	RhB	14×10^{-6}	2.41×10^{-1}	54.4	100	[45]
g-C ₃ N ₄	RhB	5×10^{-2}	6.9×10^{-8}	95	320	[46]
Spray deposited ZnO	MB	5×10^{-2}	6.9×10^{-8}	95	60	[47]
ZnO-ZnWO ₄	Crystal Violet	1×10^{-3}	2.96×10^{-8}	82	160	[48]
ZnO	RhB	4.17×10^{-5}	2×10^{-4}	8	120	[49]
6% Indium ZnO	RhB	4.17×10^{-5}	1.01×10^{-2}	76	120	[49]
γ -MnO ₂	RhB	2×10^{-5}	-	90	270	[50]
Y _{0.90} Mn _{0.10} BO ₃	RhB	1×10^{-5}	3.01×10^{-2}	93	90	Our work
Y _{0.90} Fe _{0.10} BO ₃	RhB	1×10^{-5}	2.54×10^{-2}	87	90	Our work

**Figure 11.** (a) Reusability experiment for manganese doped and (b) reusability experiment for iron doped sample.

4. Conclusions

The application of epoxide-mediated gel synthesis of crystalline π -YBO₃, transition metal doped π -YBO₃, has been demonstrated successfully. The PXRD patterns confirmed the inclusion of 10% manganese and iron in π -YBO₃. The optical and PL studies of doped samples have confirmed the presence of manganese and iron. Emission in the green region was observed in the CIE 1931 XY coordination plot for the manganese-containing sample. Magnetic susceptibility versus magnetic field data showed the ferromagnetic and antiferromagnetic behaviour for manganese and iron-doped samples. For doped samples, ferroelectric and at room temperature (300 K) were also observed. The photocatalytic properties of RhB under UV-visible irradiation in the presence of manganese and iron doped π -YBO₃, have been observed.

Author contributions

Conceptualization, PG and MS; methodology, PG; software, PG; validation, PG and MS; formal analysis, PG; investigation, PG; resources, PG; data curation, PG; writing—original draft preparation, PG; writing—review and editing, PG; visualization, PG; supervision, PG; project administration, PG; funding acquisition, MS. All authors have read and agreed to the published version of the manuscript.

Research data policy and data availability statement

The manuscript has associated data in a data repository.

Acknowledgments

The authors thank Sharda University for providing an Industrial Project Grant (SU/SF/2023/25).

Conflict of interest

The authors do the work, and have mutual consent to send it as a research paper for review. The authors do not have any conflict of interest.

References

1. Rowsell JLC, Gaubicher J, Nazar LF. A new class of materials for lithium-ion batteries: Iron (III) borates. *Journal of Power Sources* 2001; 97–98: 254–257. doi: 10.1016/S0378-7753(01)00532-8
2. Kurtzig AJ, Wolfe R, LeCraw RC, Nielsen JW. Magneto-optical properties of a green room-temperature ferromagnet: FeBO₃. *Applied Physics Letters* 1969; 14(11): 350–352. doi: 10.1063/1.1652682
3. Bither TA, Frederick CG, Gier TE, et al. Ferromagnetic VBO₃ and antiferromagnetic CrBO₃. *Solid State Communications* 1970; 8(2): 109–112. doi: 10.1016/0038-1098(70)90582-X
4. Takéuchi Y, Watanabe T, Ito T. The crystal structures of warwickite, ludwigite and pinakiolite. *Acta Crystallographica* 1950; 3: 98–107. doi: 10.1107/S0365110X50000252
5. Norrestam R, Kritikos M, Sjödin A. Manganese (II, III) oxyborate, Mn₂OBO₃: A distorted homometallic warwickite—Synthesis, crystal structure, band calculations, and magnetic susceptibility. *Journal of Solid State Chemistry* 1995; 114(2): 311–316. doi: 10.1006/jssc.1995.1049
6. Attfield JP, Clarke JF, Perkins DA. Magnetic and crystal structures of iron borates. *Physica B: Condensed Matter* 1992; 180–181: 581–584. doi: 10.1016/0921-4526(92)90401-D
7. Bertaut EF. Structures des boroferrites. *Acta Crystallographica* 1950; 3: 473–474. doi: 10.1107/S0365110X50001312
8. Li HK, Wang L, Cai GM, et al. Synthesis and crystal structure of a novel ludwigite borate: Mg₂InBO₅. *Journal of Alloys and Compounds* 2013; 575: 104–108. doi: 10.1016/j.jallcom.2013.04.024
9. Perkins DA, Attfield JP. Resonant powder X-ray determination of the cation distribution in FeNi₂BO₅. *Journal of the Chemical Society, Chemical Communications* 1991; 4: 229–231. doi: 10.1039/C39910000229
10. Fuchs B, Schröder F, Heymann G, et al. Crystal structure re-determination, spectroscopy, and photoluminescence of π-YBO₃: Eu³⁺. *Journal of Inorganic and General Chemistry* 2021; 647(22): 2035–2046. doi: 10.1002/zaac.202100229
11. Pitscheider A, Kaindl R, Oeckler O, Huppertz H. The crystal structure of π-ErBO₃: New single-crystal data for an old problem. *Journal of Solid State Chemistry* 2011; 184(1): 149–153. doi: 10.1016/j.jssc.2010.11.018
12. Lin J, Sheptyakov D, Wang Y, Allenspach P. Structures and phase transition of vaterite-type rare earth orthoborates: A neutron diffraction study. *Chemistry of Materials* 2004; 16(12): 2418–2424. doi: 10.1021/cm0499388
13. Morgan PED, Carroll PJ, Lange FF. Crystal structure of YSiO₂N and a reappraisal of the “vaterite” type, YBO₃. *Materials Research Bulletin* 1977; 12(3): 251–259. doi: 10.1016/0025-5408(77)90142-8
14. Levin EM, Roth RS, Martin JB. Polymorphism of ABO₃ type rare earth borates. *American Mineralogist: Journal of Earth and Planetary Materials* 1961; 46(9–10): 1030–1055.
15. Newnham RE, Redman MJ, Santoro RP. Crystal structure of yttrium and other rare-earth borates. *Journal of the American Ceramic Society* 1963; 46(6): 253–256. doi: 10.1111/j.1151-2916.1963.tb11721.x

16. Weir CE, Lippincott ER. Infrared studies of aragonite, calcite, and vaterite type structures in the borates, carbonates, and nitrates. *Journal of Research of the National Bureau of Standards. Section A, Physics and Chemistry* 1961; 65A(3): 173–180. doi: 10.6028/jres.065A.021
17. Weir CE, Schroeder RA. Infrared spectra of the crystalline inorganic borates. *Journal of Research of the National Bureau of Standards—A. Physics and Chemistry* 1964; 68A(5): 465–487. doi: 10.6028/jres.068A.045
18. Laperches JP, Tarte P. Infrared absorption spectra of rare earth borates (French). *Spectrochimica Acta* 1966; 22(7): 1201–1210. doi: 10.1016/0371-1951(66)80023-1
19. Kriz HM, Bray PJ. On the crystal structure of YBO_3 , a vaterite-type borate. *The Journal of Chemical Physics* 1969; 51(8): 3624–3625. doi: 10.1063/1.1672566
20. Denning JH, Boss SD. The vibrational spectra and structures of some rare-earth borates. *Spectrochimica Acta Part A: Molecular Spectroscopy* 1972; 28(9): 1775–1785. doi: 10.1016/0584-8539(72)80148-X
21. Bradley WF, Graf DL, Roth RS. The vaterite-type ABO_3 rare-earth borates. *Acta Crystallographica* 1966; 20: 283–287. doi: 10.1107/S0365110X66000549
22. Chadeyron G, El-Ghozzi M, Mahiou R, Cousseins JC. Revised structure of the orthoborate YBO_3 . *Journal of Solid State Chemistry* 1997; 128(2): 261–266. doi: 10.1006/jssc.1996.7207
23. Ren M, Lin JH, Dong Y, et al. Structure and phase transition of $GdBO_3$. *Chemistry of Materials* 1999; 11(6): 1576–1580. doi: 10.1021/cm990022o
24. Cohen-Adad MT, Aloui-Lebbou O, Goutaudier C, et al. Gadolinium and yttrium borates: Thermal behavior and structural considerations. *Journal of Solid State Chemistry* 2000; 154(1): 204–213. doi: 10.1006/jssc.2000.8837
25. Hosokawa S, Tanaka Y, Iwamoto S, Inoue M. Morphology and structure of rare earth borate ($REBO_3$) synthesized by glycothermal reaction. *Journal of Materials Science* 2008; 43: 2276–2285. doi: 10.1007/s10853-007-2023-x
26. Mahato SS, Mahata D, Panda S, Mahata S. Perspective chapter: Sol-gel science and technology in context of nanomaterials—Recent advances. *Sol-Gel Method-Recent Advances* 2023. doi: 10.5772/intechopen.111378
27. Gupta P, Sahni M, Chauhan S. Enhanced photoluminescence properties of rare earth elements doped $Y_{0.50}Gd_{0.50}BO_3$ phosphor and its application in red and green LEDs. *Optik* 2021; 240: 166810. doi: 10.1016/j.ijleo.2021.166810
28. Gupta P, Tomar R, Singh NB. Chromium-doped $Y_{0.50}Gd_{0.50}BO_3$ as an excellent photocatalytic and magnetic material. *Bulletin of Materials Science* 2021; 44: 251. doi: 10.1007/s12034-021-02541-z
29. Gu GX, Wang D, Lv XS, et al. In situ study on the structural transition in YBO_3 through Raman spectroscopy. *Materials Chemistry and Physics* 2011; 131(1–2): 274–277. doi: 10.1016/j.matchemphys.2011.09.041
30. Boonchom B, Baitahe R. Synthesis and characterization of nanocrystalline manganese pyrophosphate $Mn_2P_2O_7$. *Materials Letters* 2009; 63(26): 2218–2220. doi: 10.1016/j.matlet.2009.07.028
31. Orhan A, Aydin C, Aydin H, et al. Synthesis and optical properties of iron doped gallium nitride nanostructures by sol gel method. *Microsystem Technologies* 2015; 21: 1219–1224. doi: 10.1007/s00542-014-2273-x
32. Lever ABP. *Inorganic Electronic Spectroscopy*, 2nd ed. Elsevier; 1984.
33. You H, Zhang J, Hong G, Zhang H. Luminescent properties of Mn^{2+} in hexagonal aluminates under ultraviolet and vacuum ultraviolet excitation. *The Journal of Physical Chemistry C* 2007; 111(28): 10657–10661. doi: 10.1021/jp071889+
34. Li RK, Greaves C. $YCa_3(MnO)_3(BO_3)_4$: A manganese borate containing ferromagnetic chains on a kagomé lattice. *Physical Review B* 2003; 68(17): 172403. doi: 10.1103/PhysRevB.68.172403
35. Continentino MA, Pedreira AM, Guimaraes RB, et al. Specific heat and magnetization studies of Fe_2OBO_3 , Mn_2OBO_3 and $MgScOBO_3$. *Physical Review B* 2001; 64: 014406. doi: 10.1103/PhysRevB.64.014406
36. Sultan K, Ikram M, Gautam S, et al. Electrical and magnetic properties of the pulsed laser deposited Ca doped $LaMnO_3$ thin films on Si (100) and their electronic structures. *RSC Advances* 2015; 5(85): 69075–69085. doi: 10.1039/C5RA08028B
37. Kumari K. Magnetic and dielectric properties of Fe_3BO_6 nanoplates prepared through self-combustion method. *Journal of Advanced Dielectrics* 2017; 7(6): 1750043. doi: 10.1142/S2010135X17500436
38. Mattepanavar S, Angadi B, Rayaprol S. Low temperature magnetic studies on $PbFe_{0.5}Nb_{0.5}O_3$ multiferroic. *Physica B: Condensed Matter* 2014; 448: 229–232. doi: 10.1016/j.physb.2014.04.024
39. Rivas-Murias B, Rivadulla F, Sánchez-Andújar M, et al. Role of t_{2g} versus e_g interactions in the physical properties of A_2OBO_3 ($A = Mn, Fe$). *Chemistry of Materials* 2006; 18(19): 4547–4552. doi: 10.1021/cm0609698
40. Maignan A, Lainé F, Guesdon A, et al. Charge ordering and multiferroicity in Fe_3BO_5 and Fe_2MnBO_5 oxyborates. *Journal of Solid State Chemistry* 2017; 246: 209–213. doi: 10.1016/j.jssc.2016.11.034
41. Karmakar R, Neogi SK, Midya N, et al. Magnetic properties of Mn doped ZnO: The role of synthesis route. *Journal of Materials Science: Materials in Electronics* 2016; 27: 6371–6381. doi: 10.1007/s10854-016-4572-8

42. Ke S, Lin P, Zeng X, et al. Tuning of dielectric and ferroelectric properties in single phase BiFeO₃ ceramics with controlled Fe²⁺/Fe³⁺ ratio. *Ceramics International* 2014; 40(4): 5263–5268. doi: 10.1016/j.ceramint.2013.10.098
43. Tomar R, Abdala AA, Chaudhary RG, et al. Photocatalytic degradation of dyes by nanomaterials. *Materials Today: Proceedings* 2020; 29: 967–973. doi: 10.1016/j.matpr.2020.04.144
44. Zhong HE, Shaogui Y, Yongming JU, et al. Microwave photocatalytic degradation of rhodamine B using TiO₂ supported on activated carbon: Mechanism implication. *Journal of Environmental Sciences* 2009; 21(2): 268–272. doi: 10.1016/S1001-0742(08)62262-7
45. Su S, Guo W, Leng Y, et al. Heterogeneous activation of Oxone by Co_xFe_{3-x}O₄ nanocatalysts for degradation of rhodamine B. *Journal of Hazardous Materials* 2013; 244–245: 736–742. doi: 10.1016/j.jhazmat.2012.11.005
46. Yadav AA, Kang SW, Hunge YM. Photocatalytic degradation of rhodamine B using graphitic carbon nitride photocatalyst. *Journal of Materials Science: Materials in Electronics* 2021; 32: 15577–15585. doi: 10.1007/s10854-021-06106-y
47. Hunge YM. Photoelectrocatalytic degradation of methylene blue using spray deposited ZnO thin films under UV illumination. *MOJ Polymer Science* 2017; 1(4): 135–139. doi: 10.15406/mojps.2017.01.00020
48. Kale V, Hunge YM, Kamble SA, et al. Modification of energy level diagram of nano-crystalline ZnO by its composites with ZnWO₄ suitable for sunlight assisted photo catalytic activity. *Materials Today Communications* 2021; 26: 102101. doi: 10.1016/j.mtcomm.2021.102101
49. Pradeev Raj K, Sadaiyandi K, Kennedy A, Sagadevan S. Photocatalytic and antibacterial studies of indium-doped ZnO nanoparticles synthesized by co-precipitation technique. *Journal of Materials Science: Materials in Electronics* 2017; 28: 19025–19037. doi: 10.1007/s10854-017-7857-7
50. Moulai F, Fellahi O, Messaoudi B, et al. Electrodeposition of nanostructured γ-MnO₂ film for photodegradation of rhodamine B. *Ionics* 2018; 24: 2099–2109. doi: 10.1007/s11581-018-2440-7